ARTICLE

Beyond the Active Site: Mechanistic Investigations of the Role of the Secondary Coordination Sphere and Beyond on Multi-Electron Electrocatalytic Reactions and Their Relations Between Kinetics and Thermodynamics

Vincent C.-C. Wang[a]

The development of an electrocatalyst with a rapid turnover frequency, low overpotential and long-term stability is highly desired for fuel-forming reactions, such as water splitting and CO_2 reduction. The findings of the scaling relationships between the catalytic rate and thermodynamic parameters over a wide range of electrocatalysts in homogeneous and heterogeneous systems provide useful guidelines and predictions for designing better catalysts for those redox reactions. However, such relationships also suggest that a catalyst with a high catalytic rate is typically associated with a high overpotential for a given reaction. Inspired by enzymes, the introduction of additional interactions through the secondary coordination sphere beyond the active site, such as hydrogen-bonding or electrostatic interactions, have been shown to offer a promising avenue to disrupt these unfavorable relationships. Herein, we further investigate the influence of these cooperative interactions on the faster chemical steps, in addition to the rate-limiting step widely examined before, for molecular electrocatalysts with the structural and electronic modifications designed to facilitate the dioxygen reduction reaction, CO_2 reduction reaction and hydrogen evolving reaction. Based on the electrocatalytic kinetic analysis, the rate constants for faster chemical steps and their correlation with the corresponding thermodynamic parameters are evaluated. The results suggest that the effects of the secondary coordination sphere and beyond on these fuel-forming reactions are not necessarily beneficial for promoting all chemical steps and no apparent relation between rate constants and thermodynamic parameters are found in some cases studied here, which may implicate the design of electrocatalysts in the future. Finally, these analyses demonstrate that the characteristic features for voltammograms and foot-of-the-wave-analysis plots are associated with the specific kinetic phenomenon among these multi-electron electrocatalytic reactions, which provides a useful framework to probe the insights of chemical and electronic modifications on the catalytic steps quantitatively (i.e. kinetic rate constants) and to optimize some of critical steps beyond the rate-limiting step.

Introduction

The development of electrocatalysts for fuel-forming reactions, such as water splitting and CO_2 reduction, plays a vital role for future sustainable and renewable energy. A desired electrocatalyst is expected to have a high turnover frequency (TOF), small overpotential and high stability (turnover number). In recent years, a great amount of research efforts have been made to understand operating principles and detailed mechanisms toward these aims in both homogeneous and heterogeneous systems.[1-3] One of important findings is the scaling relationship between the catalytic rates and thermodynamic values (e.g. overpotential or binding energy between substrate and catalyst surface) found in both systems, which allows to predict the trend of electrocatalytic activity over catalysts and provides guidelines for rational designing of better electrocatalysts.[1-3] Nevertheless, such relationship implies certain constraints on the optimization of catalysts, where changes made for one step of the catalytic cycle is more favorable for the overall reaction, but results in disfavoring of other steps (the Sabatier principle). This trade-off leads to a high catalytic rate that is typically associated with a high overpotential in homogeneous molecular systems.

Take the reaction through the simple EC mechanism (E: electron transfer step and C: chemical step) of a molecular electrocatalyst as an example shown in Fig 1a. In general, to modulate the catalytic activity of a catalyst, the electronic and chemical structure of the active site could be tuned directly through a modification of electron-withdrawing or electron-donating groups. For example, the substitution with an electron-withdrawing group is expected to raise the reduction potential of a catalyst through the inductive effect to facilitate the E step. Therefore, as shown in Fig 1b, a lower overpotential

[a.] *Program of Physical Chemistry, Department of Chemistry - Ångström Laboratory, Uppsala University, Uppsala 75120 Sweden. E-mail: vincentwang64@yahoo.com.*
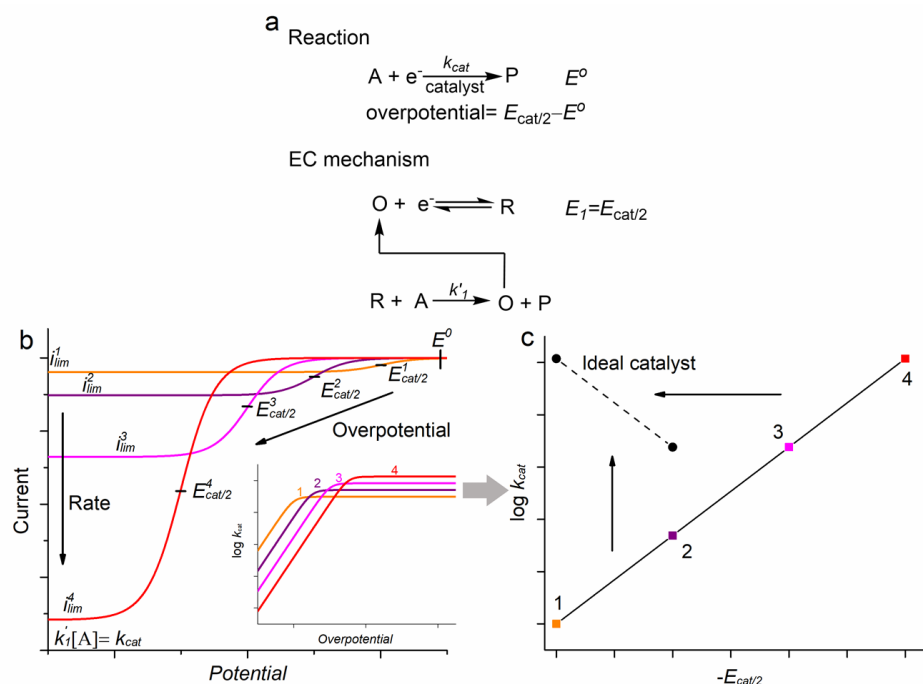
Fig 1. The illustration of a scaling relationship for the EC mechanism in the homogeneous molecular system. In the reaction scheme, A is a reactant and P is a product. O and R indicate the oxidized and reduced state of a catalyst respectively. E^0 refers to the standard reduction potential for the given reaction and E_1 is the reduction potential of a catalyst. For the EC mechanism, E_1 is equal to $E_{cat/2}$ (*vide infra*)[8] and k'_1 is the second order rate constant. Fig 1b shows typical electrocatalytic voltammograms for homogeneous molecular catalysts in a pure kinetic EC condition and their corresponding catalytic Tafel plots (*inset*). Fig 1c reveals a scaling relationship plot extracted from Fig 1b.

is required with respect to the standard reduction potential, E^0 for a given reaction. However, in the meantime, this substitution introduces a counter-balancing effect on the C step (e.g. a *positively charged* proton transfer) due to the lower electron density of the active site, which yields a lower catalytic rate. Overall, such modification yields an electrocatalyst with a low overpotential but slow TOF, as illustrated in the orange line of Fig 1b. In contrast, the substitution of an electron-donating group leads to the opposite outcome (i.e. a high overpotential but faster catalytic rate as shown in the red line of Fig 1b). Therefore, the development of new approaches to address this conundrum plays an important role in further facilitating fuel-forming reactions.

Inspired by [FeFe] hydrogenases that perform the hydrogen evolving reaction with a minimal overpotential and high TOF,[4] it has been recently demonstrated that the addition of specific functional groups to biomimetic HER catalysts at the secondary coordination sphere (SCS) to serve as proton relays near the active site can greatly facilitate fuel-forming reactions without the need to build a large overpotential into the design of the catalyst.[3, 5-7] In other words, the secondary coordination sphere, treated as an additional dimension, can be further introduced to tailor catalytic reactivity through cooperative interactions, such as electrostatic or hydrogen-bonding interactions beyond the active site. Nevertheless, so far, most reports focused on the rate-limiting step and the relationship between its kinetic rates and thermodynamic parameters (such as the reduction potential or pK_a), without considering that most reactions of

interest are multi-electron and multi-step reactions. It is important to further understand how the SCS affects other critical faster chemical steps in a catalytic cycle and their relationships between kinetic and thermodynamic properties, which could implicate overall performance, such as undesired side effects on the rate. The findings of key features and correlation between elementary reaction steps influenced by the SCS and beyond through a high degree of synthetic tunability of molecular catalysts can further provide the essence of design principles for homogeneous and heterogeneous systems in order to circumvent if not overcome the unfavourable correlation relationships.

Here, we examine molecular electrocatalysts for oxygen reduction reaction (ORR), carbon dioxide reduction reaction (CRR) and hydrogen evolving reaction (HER) reported in literature exploiting the effect of the SCS to mediate the reactions. The kinetic models for multi-electron electrocatalytic reactions, developed by Savéant and Costentin,[8] will be applied as an essential tool for kinetic analysis to determine kinetic rate constants and explore connections between kinetic and thermodynamic properties among reaction steps. Particularly, in some scenarios, the rate constant for the *faster* chemical step rather than the rate-limiting step is determined by the foot of the wave analysis (FOWA) of electrocatalytic voltammograms, which is sometimes misinterpreted in the community.[8-10]
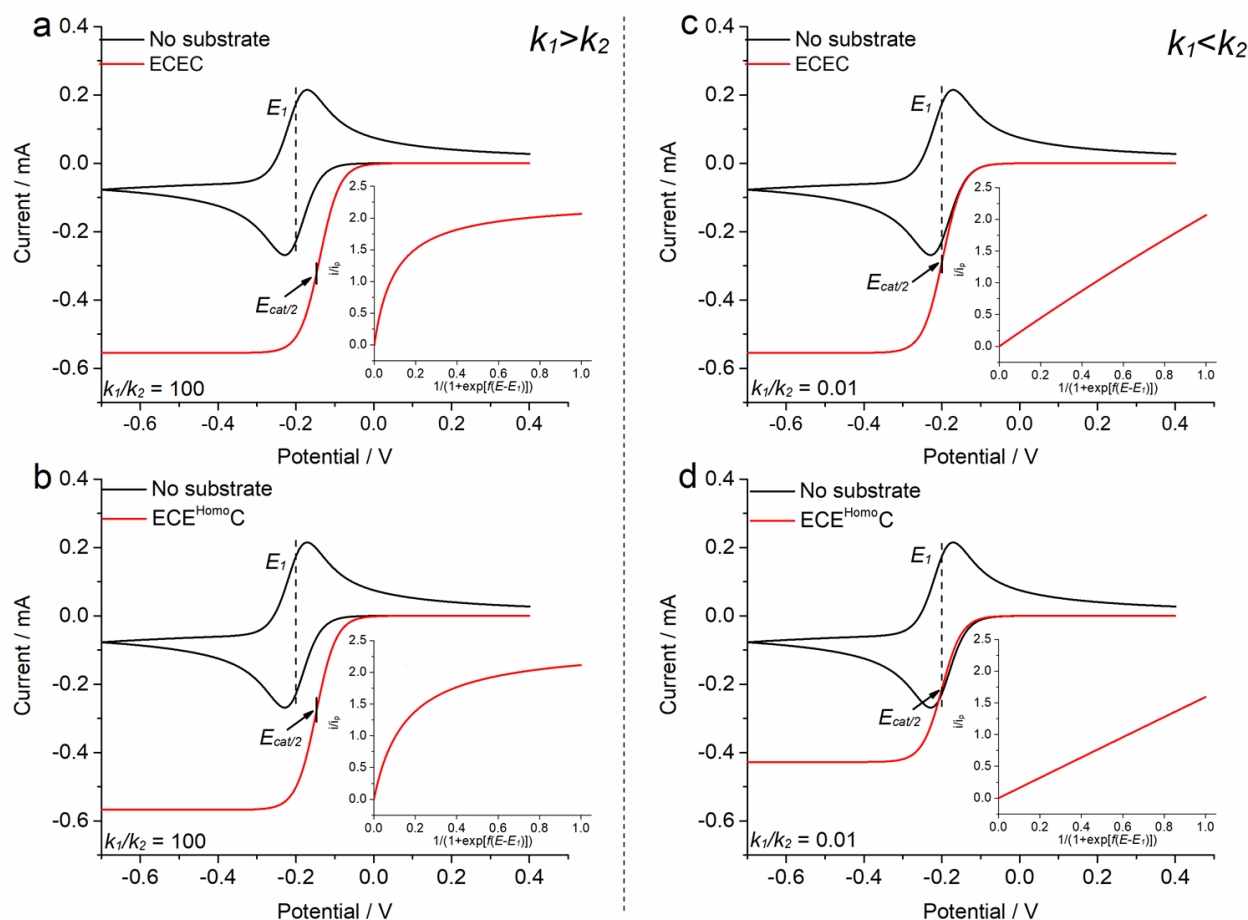
Fig 2. Electrocatalytic voltammograms and corresponding FOWA plots (inset figures) for ECEC and ECE^{Homo}C mechanism. Two different conditions for the second electron transfer are considered, ECEC and ECE^{Homo}C. For Fig 2a and 2b, (**scenario A**, $k_1>k_2$), the rate constants, k_1=100 s^{-1} and k_2=1 s^{-1} were used to obtain voltammograms. For Fig 2c and 2d, (**scenario B**, $k_1<k_2$), the rate constants, k$_1$=1 s^{-1} and k$_2$=100 s^{-1} were used. The rest parameters for simulations are E_1= −0.2 V, E_2 =0 V and the diffusion coefficient for catalysts, 10^{-5} cm^2/s. For clarity, in the black line, only the redox peak for E_1 was presented here and electrode kinetics follow the Nernstian behavior.

Results

The general guidelines for determining the kinetic and thermodynamic values from electrocatalytic voltammograms

To evaluate kinetic and thermodynamic properties of a given electrocatalyst, the electrocatalytic voltammetry is a widely used tool.[11] When a canonical electrocatalytic S-shape voltammogram is achieved as shown in Fig 1 or 2, the catalytic potential, $E_{cat/2}$ is defined at a half-wave of the potential[12] and the catalytic rate (i.e. TOF) or observed rate constant, k_{obs} for the overall reaction is determined from the limiting current, i_{lim} according to eq (1) or (2).[13, 14]

$$i_{lim} = nFSC^*\sqrt{D_{cat}k_{obs}} \quad (1), \quad \frac{i_{lim}}{i_p} = 2.24n\sqrt{\frac{RT}{Fv}}\sqrt{k_{obs}} \quad (2)$$

where i_p refers to the peak current for a redox couple of a catalyst associated with catalysis in the absence of substrate. R:

ideal gas constant, T: absolute temperature, F: Faraday constant, S: electroactive area, D_{cat}: the diffusion coefficient for the catalyst, C^*: a total concentration of electrocatalysts, n: the number of electrons involved with the reaction.

Compared to eq 1, the determination of k_{obs} by eq 2 is more straightforward due to no prior knowledge for the electroactive area and the diffusion coefficient of the catalyst. If the S-shape voltammogram is not achievable, due to side phenomena such as substrate depletion, the foot of the wave analysis can be applied to determine the catalytic rate constant.[15] However, for multi-electron redox reactions, it was found that, in some scenarios, the rate constant determined by FOWA is the *faster* chemical step rather than the rate-limiting step as expected from the EC mechanism.[8-10]

Take the most likely-encountered ECEC reaction mechanism with $E_1 < E_2$ in the reduction direction (reaction schemes as shown in Table 1) as examples shown in Fig 2 where **scenario A** refers to $k_1 >k_2$ and **scenario B** refers to $k_1<k_2$. Since the second electron transfer can either occur through the interfacial electron transfer between an electrode and catalysts or through

rapid homogeneous electron transfer among catalysts, the ECEC and $ECE^{Homo}C$ mechanism are discussed here. For a S-shape electrocatalytic voltammogram, typically, the rate constant for the rate-limiting step is directly estimated by i_{lim} (e.g. $k_{obs} \approx k_2$ for **scenario A**, and $k_{obs} \approx k_1$ for **scenario B**) since the overall rate is limited by the slowest step. Alternatively, for **scenario A**, a more precise determination of k_1 and k_2 can be achieved by the combination of eq (T2) and eq (T3) for ECEC or eq (T6) and eq (T7) for $ECE^{Homo}C$ as equations summarized in Table 1.[10] For most electrocatalytic reactions, it is expected that more than one elementary step for chemical reaction, not as shown in the reaction scheme of Table 1, are involved (such as fuel-forming reactions discussed later). Nevertheless, a single *apparent* rate constant can be used to represent a collective combination of all elementary chemical steps involved. Therefore, the rate constants, k_1 and k_2 determined by kinetic schemes shown in Table 1 can be treated as the apparent rate constant.

For the feature of a FOWA plot, the general I-V relationship depicted for ECEC (eq T1 in Table 1) can be approximated to eq 3 when **scenario A** occurs with the first formal potential, E_1 that is more negative than E_2 ($\sim$150 mV).[9] For $ECE^{Homo}C$, the general equation (eq T5) can be rearranged as eq 4. (The detailed derivation can be found in SI and ref 8, 9).

$$i = \frac{2FSC^*\sqrt{D_{cat}k_1}}{1+\varepsilon_1+\frac{\sqrt{k_1}}{\sqrt{k_2}}} \quad \text{(3) for ECEC}$$

$$i = \frac{FSC^*\sqrt{2D_{cat}k_1}}{1+\varepsilon_1+\left(\frac{\sqrt{\frac{2k_1}{k_2}-1}}{2-\frac{k_2}{k_1}}\right)} \quad \text{(4) for } ECE^{Homo}C$$

$\varepsilon_1 = \exp[f(E-E_1)]$ and E: electrode potential

Therefore, when plotting i against $(1+\varepsilon_1)$ (i.e. FOWA plot), the *curve* shape of a FOWA plot is obtained instead of a straight line expected from the EC mechanism due to the additional term, $(\sqrt{k_1}/\sqrt{k_2})$ or $[(\sqrt{2k_1/k_2}-1)/(2-k_2/k_1)]$ in the denominator from eq 3 and eq 4 respectively.[9] As a result, the rate constant determined by a FOWA plot for **scenario A** is k_1 (i.e. the faster chemical step) rather than the rate-limiting kinetic constant, k_2 that should be determined by i_{lim}.[9] In comparison, for **scenario B,** the approximate equations, eq 5 and 6 are obtained respectively for ECEC and $ECE^{Homo}C$. Therefore, the FOWA plot is expected to reveal a straight line and the rate-limiting kinetic constant is obtained from the slope.

$$i = \frac{2FSC^*\sqrt{D_{cat}k_1}}{1+\varepsilon_1} \quad \text{(5) for ECEC}$$

$$i = \frac{FSC^*\sqrt{2D_{cat}k_1}}{1+\varepsilon_1} \quad \text{(6) for } ECE^{Homo}C$$

The characteristic features of electrocatalytic voltammograms for these mechanisms and the corresponding FOWA plots are demonstrated in Fig 2 and summarized in Table 1. The key different features between **scenario A** and **B** are that an anodic

shift of the $E_{cat/2}$ value of electrocatalytic voltammograms with respect to E_1 and the curve shape of the corresponding FOWA plots are observed for **scenario A** as shown in Fig 2a-b. In other words, as the concentration of substrate A increases, the anodic shift of a voltammogram is expected for $k_1 > k_2$. It is worth noting that even *in the presence of substrate depletion*, such key features still can be observed since negligible side phenomena are expected in the region of low overpotential.[9] These results suggest that the feature of FOWA plots can be used to probe mechanistic insights. In addition, the k_1 value determined by FOWA is sensitive to the difference between E_1 and E_2 (for ECEC) and the ratio of k_1/k_2.[9] Alternatively, the k_1 value can be estimated through $E_{cat/2}$ that varies with the ratio of $(\sqrt{k_1}/\sqrt{k_2})$ (Table 1) in the **scenario A**. Therefore, Table 1 is used as guidance to characterize the reaction mechanism and obtain the corresponding apparent rate constant in the following case studies.
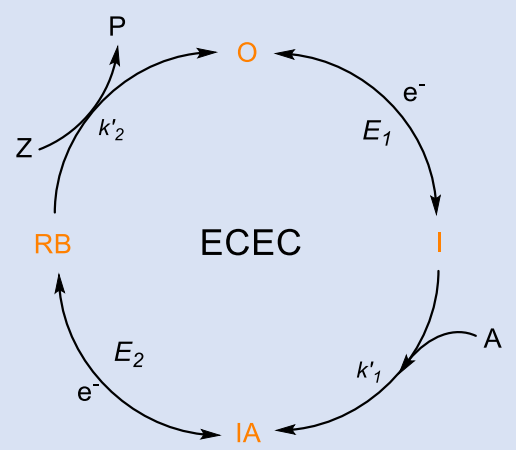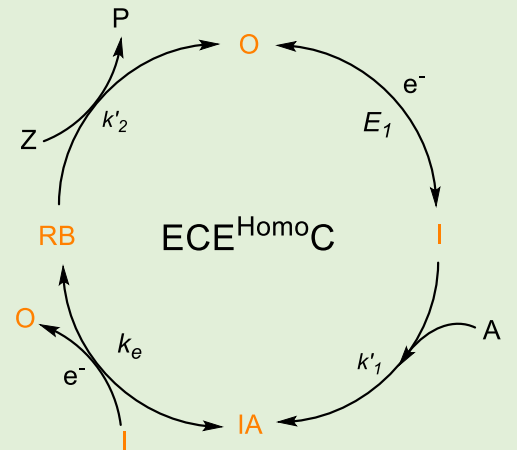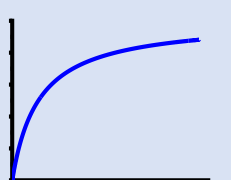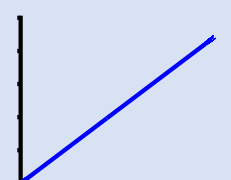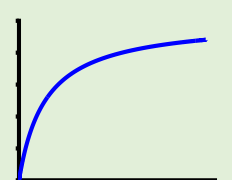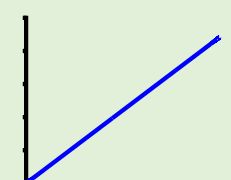
Case studies
Case A: Oxygen reduction reaction (ORR)

Recently, a series of Fe tetraphenylporphyrin (FeTPP) derivatives has been prepared by the Mayer group to investigate their catalytic mechanisms for ORR and the effect of the SCS through judicious designs of porphyrin ligands.[16-20] All reported rate constants for these complexes were determined by FOWA, which they referred to as the rate-limiting step for the first proton transfer as shown in Scheme 1 (eq $(5)_{ORR}$) following sequential EC steps. However, re-examinations of voltammograms and FOWA plots suggest that the rate constant determined by FOWA is *not* the rate-limiting step and instead should be assigned to the first *fast* chemical step as suggested in the Table 1. The most prominent evidence to support this new interpretation is that all FOWA plots reported from ref 16-18 have a *curve* shape. Furthermore, the appreciable extent of the anodic shift of voltammograms (or the anodic shift of the pseudo $E_{cat/2}$) was observed as the concentration of the proton source was increased (i.e. the pseudo first order rate constant increased). These features clearly indicate that the rate constant determined by FOWA is not the rate-limiting step. In stark contrast, the same FeTPP complex was also shown to be capable of catalyzing the reduction of CO_2 to CO, in which the FOWA plot revealed a straight line (e.g. Ref 16 for ORR vs ref 21 for CRR) because k_1^{CRR} is much smaller than k_2^{CRR}, which indicates the rate constant determined by FOWA for CRR is the rate-limiting step. (*vide infra*)
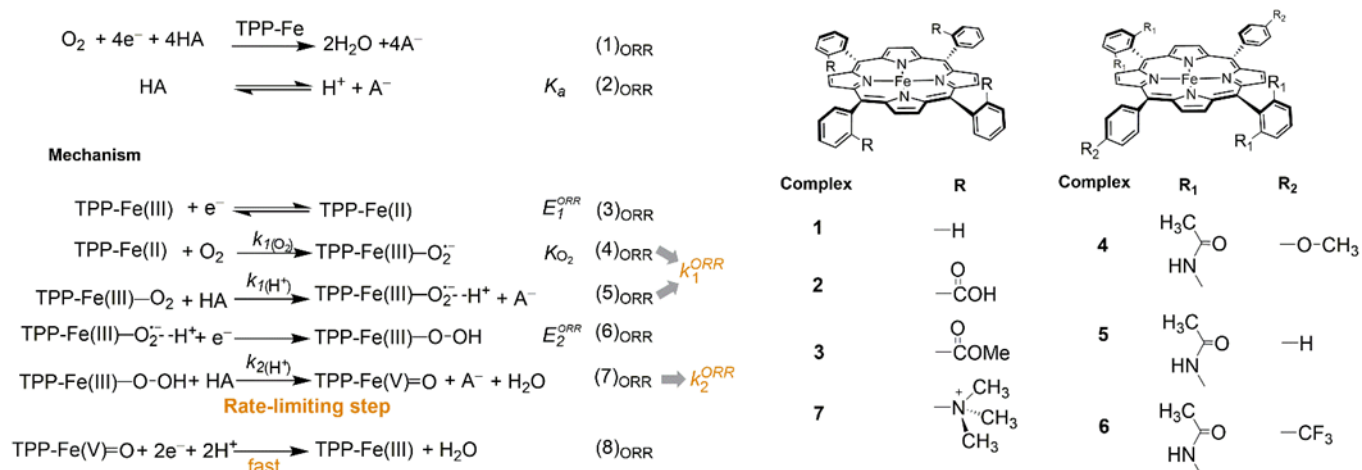
Therefore, the rate constant determined by FOWA for ORR meditated by the Fe(TPP) complex is re-assigned as an apparent rate constant, k_1^{ORR} that represents a collection of faster chemical steps between the first and second E step as shown in Scheme 1 (i.e. the combination of eq (4)-(5)$_{ORR}$). The k_1^{ORR} value is likely to be greatly affected by the first proton transfer step (eq (5)$_{ORR}$) as suggested.[16, 18, 19] For the rate constant of the rate-limiting step, k_2^{ORR}, this value is proposed to be associated with the reaction of the O-O bond breaking step (eq (7)$_{ORR}$), which thereby should be determined by i_{lim}. Reanalysis of voltammograms from ref 16 to determine k_2^{ORR} through i_{lim} afforded the third order rate constant, k_{or}, 9.6 x 10^5 $M^{-2}s^{-1}$

Table 1. Summary of key features for ECEC mechanism.

Thermodynamic parameters	[a] $E_1 < E_2$ (Nernstian electron transfer)			
[b]*Mechanism*	**ECEC** *FOWA-axis: $1/(1 + \varepsilon_1)$*		**ECE^{Homo}C** (Rapid second electron transfer in solution) *FOWA-axis: $1/(1 + \varepsilon_1)$*	
General equation	$i = \dfrac{2SFC^*\sqrt{D_{cat}}}{\frac{1}{\sqrt{k_1}}+\frac{\varepsilon_1}{\sqrt{k_1}}+\frac{1}{\sqrt{k_2}}+\frac{\varepsilon_2}{\sqrt{k_2}}}$ (eq T1) $k_{obs} = \left(\dfrac{\sqrt{k_1}\sqrt{k_2}}{\sqrt{k_1}+\sqrt{k_2}}\right)^2$ (eq T2)		$i = \dfrac{SFC^*\sqrt{2D_{cat}}}{\frac{1}{\sqrt{k_1}}+\frac{\varepsilon_1}{\sqrt{k_1}}+\frac{1}{\sqrt{k_1}}(\frac{\sqrt{\frac{2k_1}{k_2}}-1}{2-\frac{k_2}{k_1}})}$ (eq T5) $k_{obs} = \dfrac{0.5k_1(2-\frac{k_2}{k_1})^2}{\left(1-\frac{k_2}{k_1}+\sqrt{\frac{2k_1}{k_2}}\right)^2}$ (eq T6)	
	$k_1 > k_2$	$k_1 < k_2$	$k_1 > k_2$	$k_1 < k_2$
Characteristic feature of FOWA plots				
[c]*Kinetic information*	k_1 from FOWA k_2 from i_{lim} *Sensitive to [d]ΔE, i.e. great errors in k_1 calculated from FOWA for $\Delta E < 150$ mV.* $k_{obs} \approx k_2$ $E_{cat/2} = E_1 + \frac{1}{f}\ln\left(1 + \sqrt{\frac{k_1}{k_2}}\right)$ (eq T3)	k_1 from FOWA or i_{lim} *Less sensitive to ΔE, i.e. small errors in k_1 calculated from FOWA for $\Delta E < 60$ mV.* $k_{obs} \approx k_1$ $E_{cat/2} \approx E_1$ (eq T4)	k_1 from FOWA k_2 from i_{lim} *Small errors in k_1 calculated from FOWA* $k_{obs} \approx k_2$ $E_{cat/2} = E_1$ $+\frac{1}{f}\ln\left(1 + \left(\frac{\sqrt{\frac{2k_1}{k_2}}-1}{2-\frac{k_2}{k_1}}\right)\right)$ (eq T7)	k_1 from FOWA or i_{lim} *Negligible errors in k_1 calculated from FOWA.* $k_{obs} \approx 0.5k_1$ $E_{cat/2} \approx E_2$ (eq T8)

[a] For ECEC with $E_1 > E_2$, results between $k_1 > k_2$ and $k_1 < k_2$ are exchanged since the ECEC mechanism can be regarded as two individual EC reactions.[9]

[b]k'_1 and k'_2 are the second-order rate constants for the first and second chemical steps respectively. The pseudo first order rate constants ($k_1 = k'_1 C^o_A$; $k_2 = k'_2 C^o_Z$) are discussed here since the concentration of substrate is much higher than the one of catalysts.[8] E_1 and E_2 refer to the formal reduction potential for the first and second electron transfer respectively. k_e indicates the rapid homogeneous electron transfer between catalysts. The orange color refers to the state of a catalyst in the catalytic cycle. O: oxidized state, I: one-electron reduced state, IA and RB: one-electron and two-electron reduced substrate-bound intermediate state. A and Z : co-substrates, P : product. [c] ref 9. [d]$\Delta E = |E_1 - E_2|$.

Scheme 1. The proposed mechanism of ORR catalyzed by Fe(TPP) and the structure of its derivatives studied here

according to the overall rate law (eq 7). This value is in good agreement with the rate constant, 3.4×10^6 $M^{-2}s^{-1}$ determined from spectroscopic measurements.[16]

$$\text{The overall rate} = k_{or}[O_2][FeTPP][H^+] \quad \textbf{(7)}$$

More detailed discussions for justifying these new interpretations and assignments can be found in SI. Here, how the inductive effect through the modifications of functional groups and the effect of the secondary coordination sphere on the faster chemical steps are further examined, particularly the relation between k_1^{ORR} and the first reduction potential of Fe^{III}/Fe^{II}, E_1^{ORR}. Based on the principle of Brønsted–Evans–Polanyi, the correlation between k_1^{ORR} and free energy between eq (3)-(5)$_{ORR}$ in Scheme 1 can be described as eq 8 as discussed before.[22] Therefore, the effect of individual elementary chemical step proposed on k_1^{ORR} can be evaluated quantitively if a correlation can be obtained as depicted in eq 8.

$$\frac{RT\ln 10}{F}\log k_1^{ORR} = -\alpha_1 E_1^{ORR} - \alpha_2 \frac{RT\ln 10}{F} pK_a + \alpha_3 \frac{RT}{F} \ln K_{O_2} + C \quad (8)$$

where α_1, α_2 and α_3 are a correlation coefficient that is respectively associated with E_1^{ORR} for redox couple of Fe^{III}/Fe^{II}, the pK_a value for the acid used for the ORR and the binding constant, K_{O_2} between molecular oxygen and the Fe(TPP) derivative. C is a constant.

Fig 3 shows a linear correlation between $\log (k_1^{ORR})$ and E_1^{ORR} from complex **2-7** in the presence of DMF-H$^+$ as proton source, which suggests that these complexes operate within the same mechanism depicted for the faster chemical steps, eq (4)-(5)$_{ORR}$. For complex **4-7**, the complex with a more negative E_1^{ORR} value, induced by electron-donating groups, facilitated the proton transfer step (eq (5)$_{ORR}$), which follows the scaling relationship discussed earlier. Unexpectedly, the complex **2-3** modified with strong electron-withdrawing groups revealed a high overpotential with a high k_1^{ORR} value. More interestingly, very recently, a reverse scaling relationship between k_1^{ORR} and the free energy (i.e. the combination of E_1^{ORR} and pK_a) has been found as shown in the red line in Fig 3 with the FeTPP derivative modified with a positive-charge trimethylanilinium group, **7** when various carboxylic acids were
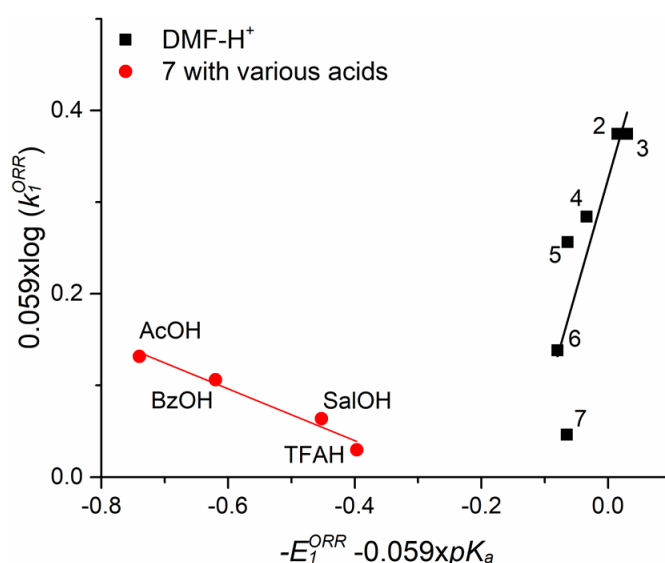

Fig 3. The relation between log (k_1^{ORR}) and the free energy for ORR catalyzed by FeTPP derivatives. The values for complex 2-6 are obtained from ref 17 and the values for complex 7 and red points are from ref 20. For black points, 20 mM [DMF-H]OTf (pK_a=6.1) was used as proton source. For red data points, 0.1 M buffer of AcOH, acetic acid (pK_a=23.5); BzOH, benzoic acid (pK_a=21.5); SalOH, salicylic acid (pK_a=16.7); and TFAH, trifluoroacetic acid (pK_a=12.6) were used as proton source respectively and the complex 7 was employed as the catalyst for ORR. All data were collected in dimethylformamide (DMF) at 1 atm of O_2.

used as proton source. As expected, such modification yielded a more positive E_1^{ORR} (the bottom-left point in the black line of Fig 3) with a small k_1^{ORR} value, due to the withdrawing substituent, in the presence of non-carboxylic DMF-H$^+$ as proton resource. Nevertheless, the substituent greatly increased the binding affinity with the negative conjugate base ion that is associated with the carboxylic acids used for ORR. As

a result, a much more negative E_1^{ORR} value was required for the reactivation of conjugate-base bound **7** adduct for the reduction of a Fe(III)/Fe(II) redox couple and ORR, thereby increasing the k_1^{ORR} value (red line in Fig 3). Interestingly, from the thermodynamic point of view, the effect on k_1^{ORR} from the more negative reduction potential required for the conjugate base-**7** adduct complex outweighs a lower driving force from a much weaker carboxylic acid used compared to DMF-H⁺ (The pK$_a$ value for acid shown in Fig 3 caption). Finally, it is worth pointing out that the rate law for the overall reaction is equal to the combination of eq (3)-(5)$_{ORR}$ in Scheme 1.[16] Nevertheless, it is interesting to examine how these derivatives affect the rate-limiting step, O-O bond breaking in the future, particularly with the modification of the carboxylate groups which aim to act as proton relay or stabilize the intermediate species through hydrogen-bonding interactions.

Case B. CO₂ reduction reaction

To further demonstrate how the key feature of voltammograms and FOWA plots can be useful to gain mechanistic insights, we briefly compare case A to the same Fe(TPP) complex that has also been displayed to catalyze the reduction of CO₂ to CO by Savéant, Costentin, Robert and their co-workers. [15, 21, 23-28] The catalytic reaction take places after the reduction of Fe(I) to Fe(0) in Fe(TPP) as shown in Scheme 2 and the reaction mechanism follows ECE^{HomoC}. As demonstrated in a series of papers from these authors,[21, 24] the FOWA plots obtained from these derivatives exhibited a straight line, which indicates that the apparent rate constant, k_1^{CRR} determined by FOWA is the rate-limiting step as a function of rate constants collectively combined from eq (4)-(6)$_{CRR}$ in Scheme 2. According to Table 1, the apparent rate constant for the faster chemical step, k_2^{CRR} can be ascribed to the rapid release of CO product (eq (7)$_{CRR}$).

In addition, a correlation between log(k_1^{CRR}) and E_1^{CRR} among FeTPP derivatives was found as shown in Fig 4[21, 28] where the black line exhibits a series of fluorine-substituted FeTPP derivatives (**8-10,** the corresponding chemical structures can be found in SI). As a number of fluorine atoms incorporated into the phenyl group increased, the E_1^{CRR} value shifted toward more positive due to a stronger electron-withdrawing property but the corresponding rate constant became smaller.[28] Two different approaches have been applied to exploit the effect of SCS on complex **1**: hydrogen-bonding/proton relay (red line)[24-26] and electrostatic interactions (blue line).[27] For the hydrogen-bonding interactions/proton relay, the introduction of hydroxyphenyl substituents to Fe(TPP), **11-12**, have been
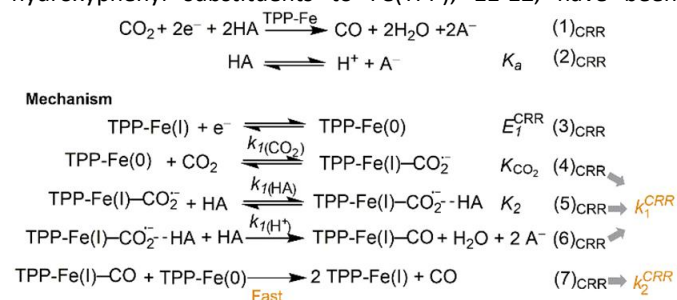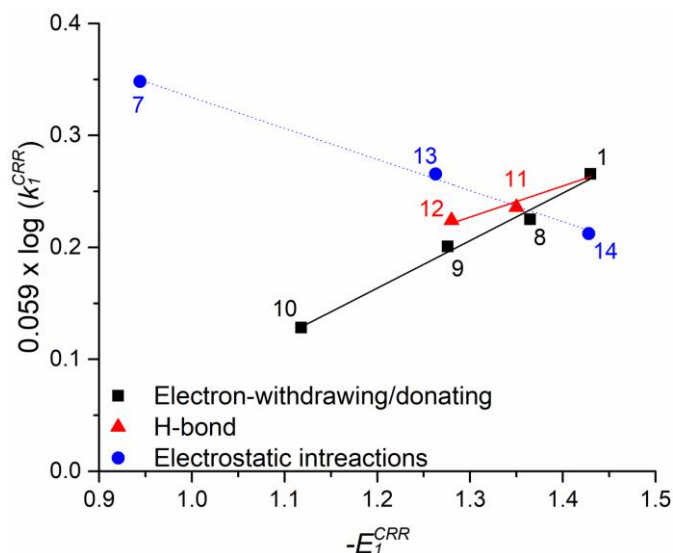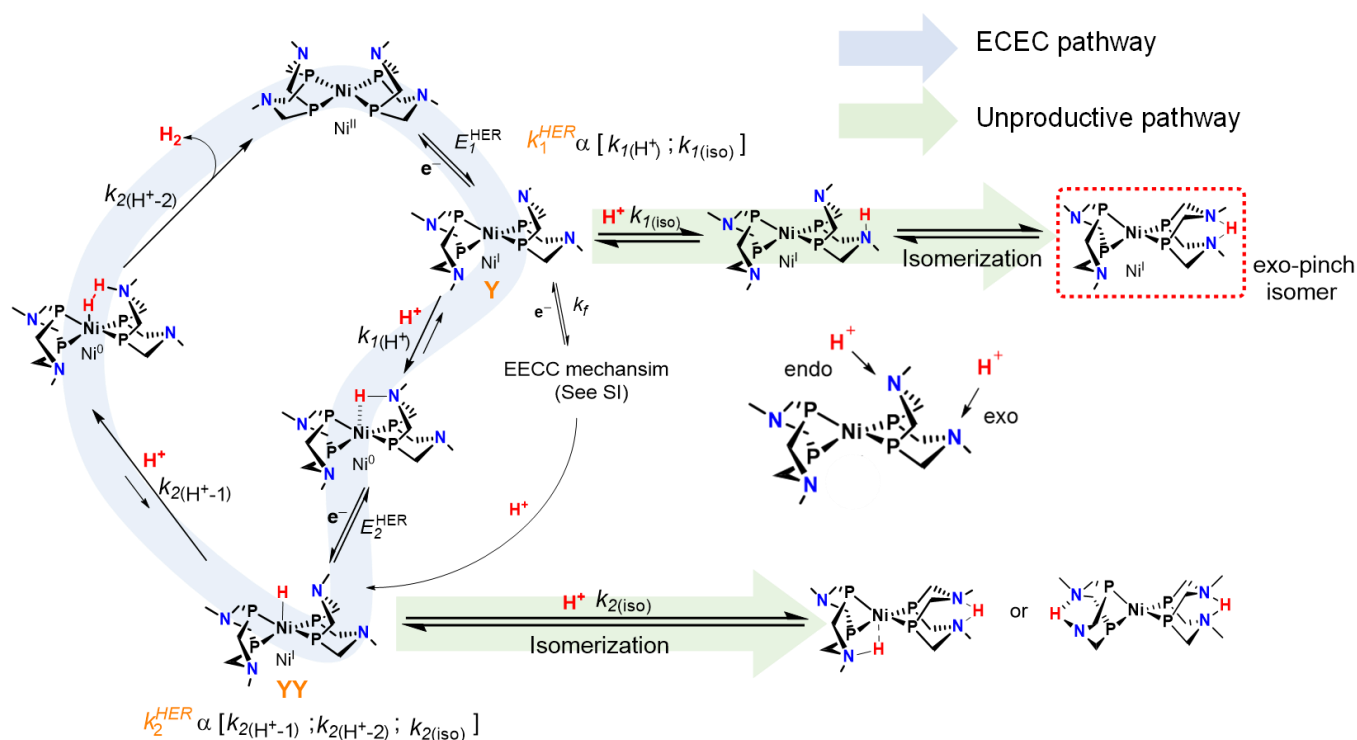

Fig 4. The relation between log(k_1^{CRR}) and E_1^{CRR} among Fe(TPP) derivatives. The values of **1** is obtained from ref 21. The values of **8-10** is obtained from ref 28. The values of **11-12** is obtained from ref 25-26. The value of **7** and **13-14** is obtained from ref 27. All experimental conditions were performed with 0.23 M CO₂ and 3 M phenol in DMF. The E_1^{CRR} value for Fe(I)/Fe(0) redox couple is determined in the absence of CO₂ and phenol. The corresponding chemical structure can be found in SI.

shown to stabilize the CO₂-bound intermediate species through hydrogen-bonding. Consequently, the catalytic rate increased (blue line vs black line) although the mechanism is different from scheme 2.[25] In comparison, the modification of charge substituents on the phenyl group of FeTPP (**7, 13-14**) to stabilize the negative-charge intermediate state (eq (4)-(5)$_{CRR}$) through the electrostatic interactions revealed a remarkable enhancement of catalytic activity.[27] The positive-charge substituent derivatives (**7** and **13**) not only shifted E_1^{CRR} to be more positive but also increased the rate constant as opposed to the negative-charge substituent, **14**. More interestingly, the strategy through electrostatic interactions seemingly reveal a reverse scaling relationship. The complex **7** stands as the best Fe porphyrin complex for CO₂ reduction to CO reported in literature in terms of the rate with a given overpotential reported so far.[29]

Case C. Hydrogen evolution Reaction (HER)

Inspired by [FeFe] hydrogenases, the [Ni-(P$^R_2$N$^{R'}_2$)₂]²⁺ derivatives developed by the Dubois group and then Pacific Northwest National Laboratory demonstrated that the introduction of pendant amines as proton relay into the Ni-bis(diphosphine) derivatives plays a key role in enhancing the activity of HER and hydrogen oxidation reaction. [5, 6, 10, 30-34] As blue highlighted in Scheme 3, the catalytic cycle for H₂ evolution has been proposed through ECEC mechanism with k_1^{HER} >k_2^{HER}. Here, the apparent rate constant, k_1^{HER} and k_2^{HER} can be regarded as a function of a collection of the rate constants of proposed productive and unproductive steps as exhibited in Scheme 3. More recently, the EECC mechanism has been further suggested to occur when a high overpotential is applied.[10, 35, 36] The S-

$$CO_2 + 2e^- + 2HA \xrightarrow{TPP\text{-}Fe} CO + 2H_2O + 2A^- \quad (1)_{CRR}$$

$$HA \rightleftharpoons H^+ + A^- \qquad K_a \quad (2)_{CRR}$$

Mechanism

$$TPP\text{-}Fe(I) + e^- \rightleftharpoons TPP\text{-}Fe(0) \qquad E_1^{CRR} \quad (3)_{CRR}$$

$$TPP\text{-}Fe(0) + CO_2 \xrightarrow{k_{1(CO_2)}} TPP\text{-}Fe(I)\text{-}CO_2^- \qquad K_{CO_2} \quad (4)_{CRR}$$

$$TPP\text{-}Fe(I)\text{-}CO_2^- + HA \xrightarrow{k_{1(HA)}} TPP\text{-}Fe(I)\text{-}CO_2^- \cdot HA \qquad K_2 \quad (5)_{CRR} \; k_1^{CRR}$$

$$TPP\text{-}Fe(I)\text{-}CO_2^- \cdot HA + HA \xrightarrow{k_{1(H^+)}} TPP\text{-}Fe(I)\text{-}CO + H_2O + 2\,A^- \quad (6)_{CRR}$$

$$TPP\text{-}Fe(I)\text{-}CO + TPP\text{-}Fe(0) \xrightarrow{Fast} 2\,TPP\text{-}Fe(I) + CO \quad (7)_{CRR} \; k_2^{CRR}$$

Scheme 2. The mechanism of CRR catalyzed by Fe(TPP).

Scheme 3. The ECEC mechanism of HER mediated by [Ni-(P$^R_2$N$^{R'}_2$)$_2$]. The blue highlight refers to the ECEC mechanism for HER. The green highlights refer to the unproductive pathways that compete with the ECEC mechanism to generate the inactive pinched isomers (e.g. the species squared by the red dot) *via* protonation on the exo-position N atom. For clarity, the detailed mechanism of EECC is omitted and the full proposed mechanism can be found in the SI. The contribution of k_f from the EECC mechanism on k_1^{HER} is negligible because ECEC is the dominant mechanism discussed here.

shape electrocatalytic voltammograms were obtained for most of the [Ni-(P$^R_2$N$^{R'}_2$)$_2$]$^{2+}$ derivatives studied under the substrate-saturated condition, which allows directly to estimate the apparent rate constant for the rate-limiting step, k_2^{HER} through i_{lim}. For the faster apparent rate constant, k_1^{HER}, the value can be estimated through eq T3 in Table 1 with the input of reported $E_{cat/2}^{HER}$ and k_2^{HER} values. Although the EECC mechanism is the dominant pathway for HER near the region of i_{lim}, the apparent rate constant, k_2^{HER}, represented for a collection of the pathways for the second chemical step between the ECEC and EECC mechanism, is the same (i.e. the same reaction pathway after the key intermediate YY as shown in scheme 3). Therefore, the k_2^{HER} value is likely to be similar between two mechanisms, which has been shown recently.[10] In addition, the half-wave potential $E_{cat/2}^{HER}$ has been shown to be only associated with the ECEC mechanism.[10]

As shown in Scheme 3, the branch and unproductive pathways (green highlights) participating with the protonation process at the exo position of pendant amine than the endo site, have been known to be detrimental to catalytic activity.[37] The boat-chair isomerization occurs through intramolecular proton transfer to generate the *inactive* exo-pitch protonated species (as shown by the red-dot square in scheme 3), which is kinetically favored and thermodynamically more stable compared to the active endo protonated species. [6, 35 37] Therefore, the k_1^{HER} and k_2^{HER} value, as a function of these isomerization pathways (i.e. $k_{1(iso)}$ and $k_{2(iso)}$ shown in Scheme 3

respectively), are expected to reflect the influence of these undesired pathways.

To further explore the influence of the active site and SCS on the electrocatalytic mechanism for HER mediated by the [Ni-(P$^R_2$N$^{R'}_2$)$_2$] complex, the modifications of the parent complex **15** were conducted in two different directions: the substituent on the P atom that coordinates to the Ni atom, is supposed to directly manipulate the electronic and chemical properties of the active site.[31, 32] In comparison, the modifications on the N atom of the [Ni-(P$^R_2$N$^{R'}_2$)$_2$] complex could lead to further clues on the role of the secondary coordination sphere.[30] As the black line shown in Fig 5b, the modifications of phosphine with less bulky substituents, **16** and **17** (Fig 6) yielded to the more negative E_1^{HER}, which is associated with the higher k_2^{HER} value compared to bulky substitutions, **18** and **19**. As opposed, when varying the acidity of pendant amines through electron-donating/withdrawing substitutions at the para position of the phenyl group (**20**-**23**), the k_2^{HER} value increased as the pK_a value of the protonated pendant amine decreased.[30] Intriguingly, at the same time, due to the inductive effect of these substitutions, the more electron-withdrawing derivative led to shift E_1^{HER} (e.g. **23**) toward the more positive value. Therefore, a reverse linear relationship is obtained as shown in the red line in Fig 5b. In contrast, no apparent (or weak) correlation between E_1^{HER} and k_1^{HER}, is found as shown in Fig 5a. Overall, the enhancement of the overall activity through these modifications were not apparent as compared to the parent complex **15** and the difference between k_1^{HER} and k_2^{HER} in the
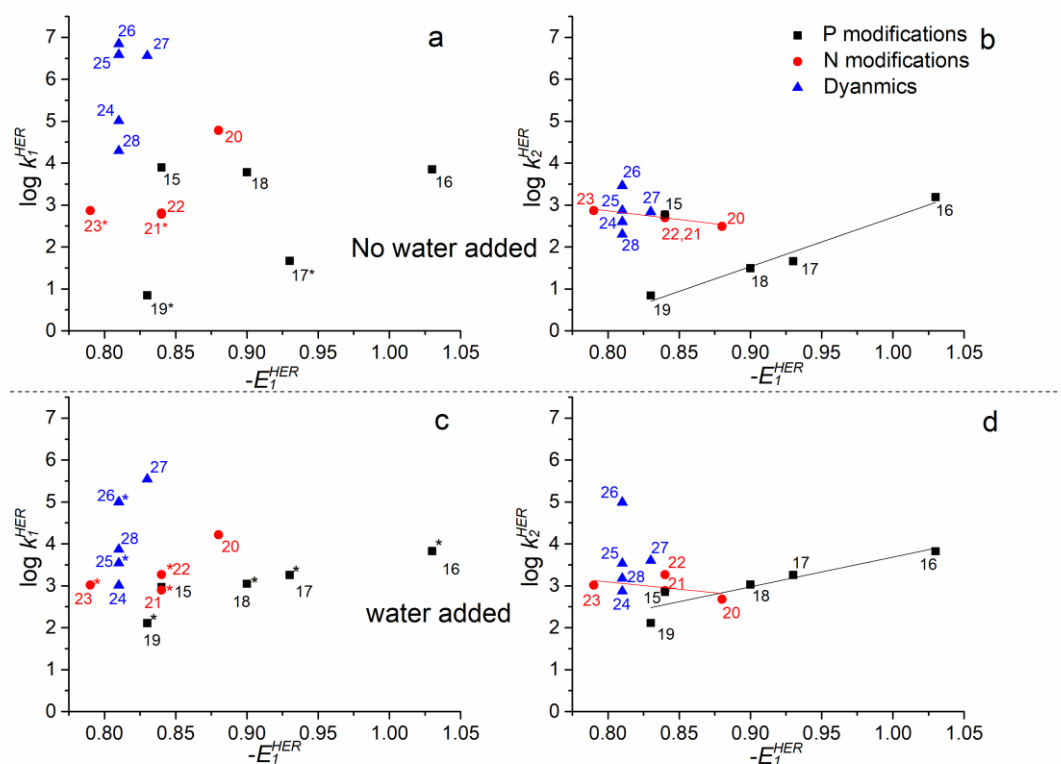
Fig 5. The relation between log (k_1^{HER}) / log (k_2^{HER}) and E_1^{HER} among [Ni-(P$^R_2$N$^{R'}_2$)$_2$]$^{2+}$ derivatives in the absence of water (a,b) and presence of water (c,d). The k_2^{HER} and $E_{cat/2}^{HER}$ values of the Ni complexes were collected from literature as below: complex **15** from ref 5; complex **16** from ref 32; complex **17**-**19** from ref 31; complex **20**-**23** from ref 30 and complex **24**-**28** from ref 33. All the values were collected in dry acetonitrile using DMF-H$^+$ as proton source. The asterisk sign indicates that the reported value, $E_{cat/2}^{HER}$ is equal or slightly negative than E_1^{HER}, which suggests the difference between the two apparent rate constants is very small. Therefore, the value for k_1^{HER} is assumed to be the same as k_2^{HER}.

most derivatives is around the range of an order of magnitude. These results are probably due to the influence of the unproductive processes for the formation of the inactive exo-pitch protonated species. According to theoretical calculations, these inactive pathways are kinetically more favorable for both key intermediate species Y and YY in Scheme 3. [33] [35]

To decrease the rate of the unproductive pathways, recently, the long n-alky chains and bulky substitutions on [Ni-(P$^R_2$N$^{R'}_2$)$_2$] (**24**-**28**) were incorporated at the *para* position of the phenyl group of the N atom of the parent complex **15**, to minimize the process of chair-boat isomerization processes through the steric effects without greatly affecting the electronic structure of the active site (i.e. the reduction potential of E_1^{HER} of **24-28** compared to **15**).[33] Consequently, the rate constant k_2^{HER} for these substituents increased were observed with a lower overpotential required for HER (blue dots in Fig 5b). In comparison, such modifications have much more prominent impact on k_1^{HER}, where the values increased with several orders of magnitude compared to the modifications described in the previous section (i.e. blue dots vs black/red dots in Fig 5a). These results suggest that the intermediate species, Y in Scheme 3 is greater affected by the unproductive protonation processes at the exo position than the intermediate species, YY.
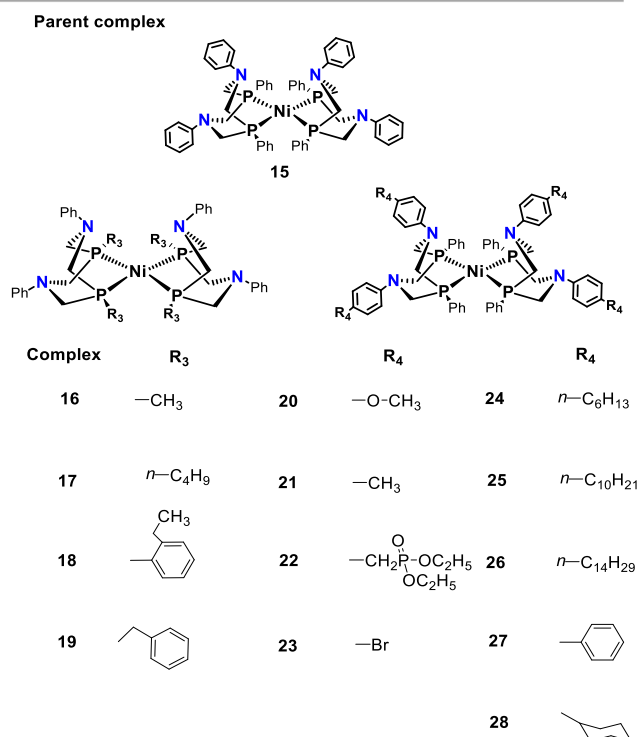

Fig 6. The chemical structure of [Ni-(P$^R_2$N$^{R'}_2$)$_2$]

ARTICLE

Finally, the addition of protic solvent as cosolvent to facilitate proton transfer was found to further enhance catalytic activity. For example, in the presence of water as cosolvent, the k_2^{HER} for the rate-limiting step increased as shown in Fig 5d compared to Fig 5b. However, the more negative $E_{cat/2}^{HER}$ values (i.e. higher overpotential) were observed concomitantly in the presence of water, which indicates that the difference between k_1^{HER} and k_2^{HER} becomes small. For the most derivatives, the k_1^{HER} values are very close to k_2^{HER}, suggesting that unproductive protonation processes associated with $k_{1(iso)}$ are accelerated in the presence of cosolvent as well, which show no apparent effect on k_1^{HER} values compared to the absence of cosolvent. In brief, these two strategies highlight the importance of the roles even beyond the secondary coordination sphere, which could have different impacts on different chemical steps.

Discussion

Here, we show that the rate constants for different chemical steps of multi-electron redox reactions can be disentangled by the analysis of electrocatalytic voltammograms and FOWA plots, in which the correlation between the apparent rate constants and thermodynamic parameters can be examined. Particularly, unlike a general conception in the community, FOWA actually leads to the rate constant for a faster chemical step rather than a rate-limiting step in some kinetic scenarios (Table 1). Therefore, the role of the SCS and beyond on the faster chemical steps for fuel-forming reactions can be further examined, which provide quantitative structure activity relationship. Although the value evaluated here are apparent rate constants, the elaborate experimental designs (such as variation of substrate/cosubstrate concentration) with kinetic analysis allow to further determine the intrinsic rate constant related to the corresponding elementary step proposed. Such practices have been recently showcased for FeTPP derivatives for CRR reaction[21, 25, 26] and MnTPP for ORR[38]. In addition, although the redox reactions investigated here are involved with the ECEC-type mechanism, other kinetic mechanisms (such as EECC) have been shown to have their own characteristic features of FOWA plots that are also associated with the specific kinetic phenomena.[8, 9]

As for the fuel-forming reactions investigated here, the results suggest that not all chemical steps are facilitated through the modification of the SCS and directly correlated with the corresponding reduction potential. For example, it would be expected that the k_1^{HER} value of a series of [Ni-($P^R_2N^{R'}_2$)$_2$]$^{2+}$ derivatives should have a correlation with the corresponding E_1^{HER} as observing a linear relation between k_1^{ORR} and E_1^{ORR} in ORR. The lack of a correlation between k_1^{HER} and E_1^{HER} can be ascribed to the inactive protonation processes for [Ni-($P^R_2N^{R'}_2$)$_2$]$^{2+}$ derivatives, which greatly disrupts the expected relation between kinetic and thermodynamic values. On the other hand, finding a free energy relationship between k_1^{ORR} and E_1^{ORR} can provide useful guidelines to further modify the SCS to facilitate chemical steps beyond the rate-limiting step. Overall, these kinetic analyses can help dissect chemical steps

to broaden the understanding of catalytic mechanism into catalyst optimization.

Finally, how do lessons learned from homogeneous molecular electrocatalysts translate to heterogeneous thin-film electrocatalysts? For most of thin-film electrocatalysts, the scaling relationships found are derived from the studies of the active site alone without considering the effect of the SCS and beyond.[39-43] In terms of the catalytic mechanism, both systems are expected to share similar essential pathways on the atomic level. Finding key features from the studies of molecular systems with the influence of the SCS and beyond can provide new insights to further tailor thin-film electrocatalysts to break down the scaling relationship. For example, recently, the presence of a high concentration of cations in the reaction environment has shown to greatly facilitate the electrocatalytic activity of heterogeneous metal electrocatalysts for CO_2 reduction due to electric field interaction provided by these ions to stabilize the intermediate species.[44-47] Such influence can be regarded as the effect of the secondary coordination sphere, which is similar to the results showcased from case B discussed here. Nevertheless, the key success to transform these findings to electrocatalysts lies in introducing a right kind of interaction from the SCS and in locating it at the relevant distance to effectively optimize the active site for electron transfer and chemical steps. At the moment, knowledge and predictive power on these aspects for these fuel-forming reactions is still lacking. Therefore, molecular electrocatalysts play an important frontline role in exploring these uncharted territories.

Conclusion

In brief, we demonstrate how kinetic analysis through S-shape electrocatalytic voltammograms and FOWA plots can be applied to identify reaction mechanism and determine rate constants for multi-electron redox reaction. Therefore, the influence of the SCS and beyond on the separately chemical steps are able to further explore quantitatively, revealing how these additional interactions affect the different stages of the reaction. The results and analysis demonstrated here provide further evaluations of the effect of these supernumerary interactions and fresh ideas for the optimization of a desired electrocatalyst to facilitate fuel-forming reaction beyond the active site.

Conflicts of interest

There are no conflicts to declare.

Acknowledgement

References

1. Z. W. Seh, J. Kibsgaard, C. F. Dickens, I. Chorkendorff, J. K. Nørskov and T. F. Jaramillo, *Science*, 2017, **355**, eaad4998.
2. K. E. Dalle, J. Warnan, J. J. Leung, B. Reuillard, I. S. Karmel and E. Reisner, *Chem. Rev.*, 2019, **119**, 2752-2875.
3. C. Costentin and J.-M. Savéant, *Nat. Rev. Chem*, 2017, **1**, 0087.
4. F. A. Armstrong and J. Hirst, *Proc. Natl. Acad. Sci. U.S.A*, 2011, **108**, 14049-14054.
5. A. D. Wilson, R. H. Newell, M. J. McNevin, J. T. Muckerman, M. Rakowski DuBois and D. L. DuBois, *J. Am. Chem. Soc.*, 2006, **128**, 358-366.
6. W. J. Shaw, M. L. Helm and D. L. DuBois, *Biochimica et Biophysica Acta (BBA) - Bioenergetics*, 2013, **1827**, 1123-1139.
7. S. Chatterjee, K. Sengupta, B. Mondal, S. Dey and A. Dey, *Acc. Chem. Res.*, 2017, **50**, 1744-1753.
8. C. Costentin and J.-M. Savéant, *ChemElectroChem*, 2014, **1**, 1226-1236.
9. V. C. C. Wang and B. A. Johnson, *ACS Catal.*, 2019, **9**, 7109-7123.
10. E. S. Wiedner, H. J. S. Brown and M. L. Helm, *J. Am. Chem. Soc.*, 2016, **138**, 604-616.
11. E. S. Rountree, B. D. McCarthy, T. T. Eisenhart and J. L. Dempsey, *Inorg. Chem.*, 2014, **53**, 9983-10002.
12. A. M. Appel and M. L. Helm, *ACS Catal.*, 2014, **4**, 630-633.
13. R. S. Nicholson and I. Shain, *Anal. Chem.*, 1964, **36**, 706-723.
14. J. M. Saveant and E. Vianello, *Electrochim. Acta*, 1965, **10**, 905-920.
15. C. Costentin, S. Drouet, M. Robert and J.-M. Savéant, *J. Am. Chem. Soc.*, 2012, **134**, 11235-11242.
16. D. J. Wasylenko, C. Rodríguez, M. L. Pegis and J. M. Mayer, *J. Am. Chem. Soc.*, 2014, **136**, 12544-12547.
17. M. L. Pegis, B. A. McKeown, N. Kumar, K. Lang, D. J. Wasylenko, X. P. Zhang, S. Raugei and J. M. Mayer, *ACS Central Science*, 2016, **2**, 850-856.
18. M. L. Pegis, C. F. Wise, B. Koronkiewicz and J. M. Mayer, *J. Am. Chem. Soc.*, 2017, **139**, 11000-11003.
19. M. L. Pegis, D. J. Martin, C. F. Wise, A. C. Brezny, S. I. Johnson, L. E. Johnson, N. Kumar, S. Raugei and J. M. Mayer, *J. Am. Chem. Soc.*, 2019, **141**, 8315-8326.
20. D. J. Martin, B. Q. Mercado and J. M. Mayer, *Science Advances*, 2020, **6**, eaaz3318.
21. C. Costentin, S. Drouet, G. Passard, M. Robert and J.-M. Savéant, *J. Am. Chem. Soc.*, 2013, **135**, 9023-9031.
22. C. Costentin and J.-M. Savéant, *J. Am. Chem. Soc.*, 2018, **140**, 16669-16675.
23. I. Bhugun, D. Lexa and J.-M. Savéant, *J. Am. Chem. Soc.*, 1996, **118**, 1769-1776.
24. C. Costentin, S. Drouet, M. Robert and J.-M. Savéant, *Science*, 2012, **338**, 90-94.
25. C. Costentin, G. Passard, M. Robert and J.-M. Savéant, *J. Am. Chem. Soc.*, 2014, **136**, 11821-11829.
26. C. Costentin, G. Passard, M. Robert and J.-M. Savéant, *Proc. Natl. Acad. Sci. U.S.A*, 2014, **111**, 14990-14994.
27. I. Azcarate, C. Costentin, M. Robert and J.-M. Savéant, *J. Am. Chem. Soc.*, 2016, **138**, 16639-16644.
28. I. Azcarate, C. Costentin, M. Robert and J.-M. Savéant, *J. Phys. Chem. C*, 2016, **120**, 28951-28960.
29. P. Gotico, Z. Halime and A. Aukauloo, *dalton trans.*, 2020, **49**, 2381-2396.
30. U. J. Kilgore, J. A. S. Roberts, D. H. Pool, A. M. Appel, M. P. Stewart, M. R. DuBois, W. G. Dougherty, W. S. Kassel, R. M. Bullock and D. L. DuBois, *J. Am. Chem. Soc.*, 2011, **133**, 5861-5872.
31. U. J. Kilgore, M. P. Stewart, M. L. Helm, W. G. Dougherty, W. S. Kassel, M. R. DuBois, D. L. DuBois and R. M. Bullock, *Inorg. Chem.*, 2011, **50**, 10908-10918.
32. S. Wiese, U. J. Kilgore, D. L. DuBois and R. M. Bullock, *ACS Catal.*, 2012, **2**, 720-727.
33. A. J. P. Cardenas, B. Ginovska, N. Kumar, J. Hou, S. Raugei, M. L. Helm, A. M. Appel, R. M. Bullock and M. O'Hagan, *Angew. Chem. Int. Ed.*, 2016, **55**, 13509-13513.
34. C. M. Klug, A. J. P. Cardenas, R. M. Bullock, M. O'Hagan and E. S. Wiedner, *ACS Catal.*, 2018, **8**, 3286-3296.
35. M.-H. Ho, R. Rousseau, J. A. S. Roberts, E. S. Wiedner, M. Dupuis, D. L. DuBois, R. M. Bullock and S. Raugei, *ACS Catal.*, 2015, **5**, 5436-5452.
36. E. S. Rountree and J. L. Dempsey, *J. Am. Chem. Soc.*, 2015, **137**, 13371-13380.
37. M. O'Hagan, M.-H. Ho, J. Y. Yang, A. M. Appel, M. R. DuBois, S. Raugei, W. J. Shaw, D. L. DuBois and R. M. Bullock, *J. Am. Chem. Soc.*, 2012, **134**, 19409-19424.
38. G. Passard, D. K. Dogutan, M. Qiu, C. Costentin and D. G. Nocera, *ACS Catal.*, 2018, **8**, 8671-8679.
39. J. K. Nørskov, J. Rossmeisl, A. Logadottir, L. Lindqvist, J. R. Kitchin, T. Bligaard and H. Jónsson, *J. Phys. Chem. B*, 2004, **108**, 17886-17892.
40. I. C. Man, H.-Y. Su, F. Calle-Vallejo, H. A. Hansen, J. I. Martínez, N. G. Inoglu, J. Kitchin, T. F. Jaramillo, J. K. Nørskov and J. Rossmeisl, *ChemCatChem*, 2011, **3**, 1159-1165.
41. H. A. Hansen, J. B. Varley, A. A. Peterson and J. K. Nørskov, *The Journal of Physical Chemistry Letters*, 2013, **4**, 388-392.
42. V. C. C. Wang, *PCCP*, 2016, **18**, 22364-22372.
43. K. S. Exner and H. Over, *Acc. Chem. Res.*, 2017, **50**, 1240-1247.
44. M. R. Singh, Y. Kwon, Y. Lum, J. W. Ager and A. T. Bell, *J. Am. Chem. Soc.*, 2016, **138**, 13006-13012.
45. M. Liu, Y. Pang, B. Zhang, P. De Luna, O. Voznyy, J. Xu, X. Zheng, C. T. Dinh, F. Fan, C. Cao, F. P. G. de Arquer, T. S. Safaei, A. Mepham, A. Klinkova, E. Kumacheva, T. Filleter, D. Sinton, S. O. Kelley and E. H. Sargent, *Nature*, 2016, **537**, 382-386.
46. E. Pérez-Gallent, G. Marcandalli, M. C. Figueiredo, F. Calle-Vallejo and M. T. M. Koper, *J. Am. Chem. Soc.*, 2017, **139**, 16412-16419.
47. S. Ringe, E. L. Clark, J. Resasco, A. Walton, B. Seger, A. T. Bell and K. Chan, *Energy & Environmental Science*, 2019, **12**, 3001-3014.

TOC Figure